J. Mech. Phys. Solids 149 (2021) 104325

Contents lists available at ScienceDirect

Journal of the Mechanics and Physics of Solids

journal homepage: www.elsevier.com/locate/jmps

Exceptional points and enhanced sensitivity in PT-symmetric continuous elastic media

Matheus I.N. Rosa [*,1], Matteo Mazzotti [1], Massimo Ruzzene [1]

Department of Mechanical Engineering, University of Colorado Boulder, USA

ARTICLE INFO

Keywords:
PT-symmetry
Exceptional points
Continuous elastic media
Enhanced sensitivity

ABSTRACT

We investigate non-Hermitian degeneracies, also known as exceptional points, in continuous elastic media, and their potential application to the detection of mass and stiffness perturbations. Degenerate states are induced by enforcing parity-time symmetry through tailored balanced gain and loss, introduced in the form of complex stiffnesses and may be implemented through piezoelectric transducers. The introduction of external perturbations leads to a splitting of the eigenvalues, which is explored as a sensitive approach to the detection of such perturbations. Numerical simulations on one-dimensional waveguides illustrate the presence of several exceptional points in their vibrational spectrum, and conceptually demonstrate their sensitivity to point mass inclusions. Second order exceptional points are shown to exhibit a frequency shift in the spectrum with a square root dependence on the perturbed mass, which is confirmed by a perturbation approach and by frequency response analyses. Elastic domains supporting guided waves are then investigated, where exceptional points are formed by the hybridization of Lamb wave modes. After illustrating a similar sensitivity to point mass inclusions, we also show how these concepts can be applied to surface wave modes for sensing crack-type defects. The presented results describe fundamental vibrational properties of PT-symmetric elastic media supporting exceptional points, whose sensitivity to perturbations goes beyond the linear dependency commonly encountered in Hermitian systems. The findings are thus promising for applications involving sensing of perturbations such as added masses, stiffness discontinuities and surface cracks.

1. Introduction

In the broad context of wave physics and related areas, a recent focus of the scientific community at large has been the exploration of non-Hermitian (NH) systems (Ashida et al., 2020). Broadly speaking, NH systems are non-conservative due to interactions with the environment producing gain and/or loss. As such, the eigenfrequencies of NH systems are generally complex, precluding many of the well-known properties of Hermitian (conservative) systems to be directly applied. For example, the topological properties of NH systems are remarkably different from that of their Hermitian counterparts (Lee, 2016; Xiong, 2018), motivating re-classifications of topological phases for NH systems to be recently proposed (Gong et al., 2018; Shen et al., 2018; Kawabata et al., 2019). These concepts have been exploited to produce one-way wave amplification and edge localization of bulk modes (called the NH skin effect) in mechanical metamaterials with feedback interactions (Ghatak et al., 2019; Brandenbourger et al., 2019; Rosa and Ruzzene, 2020). In this context, recent studies focus on a particular class of NH systems which preserve Parity-Time (PT) symmetry and exhibit

* Corresponding author.
E-mail address: matheus.rosa@colorado.edu (M.I.N. Rosa).
[1] All the authors contributed equally to this work.

https://doi.org/10.1016/j.jmps.2021.104325
Received 3 August 2020; Received in revised form 12 December 2020; Accepted 13 January 2021
Available online 22 January 2021

exceptional points (Longhi, 2018; El-Ganainy et al., 2018; Miri and Alù, 2019). The interest in these systems has early roots in the seminal work by Bender and Boettcher (1998), where it was shown that PT-symmetric NH Hamiltonians may exhibit purely real spectra. Exceptional points are special degeneracies where two or more eigenfrequencies and eigenvectors coalesce, defining a transition from a phase where eigenfrequencies are purely real, to one where they are complex conjugates (Bender et al., 2013). Among the intriguing properties of exceptional points one finds unconventional phenomena such as unidirectional invisibility (Lin et al., 2011; Fleury et al., 2015), single-mode lasers (Feng et al., 2014), and enhanced sensitivity to perturbations (Hodaei et al., 2017; Chen et al., 2017; Xiao et al., 2019). Such sensitivity is investigated here for continuous elastic media.

This work contributes to recent efforts in exploring the role of PT symmetry in acoustics and mechanics (Zhu et al., 2014; Christensen et al., 2016; Liu et al., 2018). Notable applications include the observation of the asymmetric scattering properties around exceptional points in 1D waveguides (Fleury et al., 2015; Wu et al., 2019; Hou and Assouar, 2018), and second-order topological insulators demonstrated in acoustics (Zhang et al., 2019; López et al., 2019). More recently, exceptional points were experimentally demonstrated as vibrating modes of an elastic plate hosting two mechanical oscillators with tailored losses (Domínguez-Rocha et al., 2020), while an optomechanical accelerometer based on the enhanced sensitivity around exceptional points was also proposed (Kononchuk and Kottos, 2020). Also, based on parallels between elastodynamics and NH quantum mechanics, exceptional points and their sensitivity to point masses have been recently illustrated for bi-material elastic slabs (Shmuel and Moiseyev, 2020). These works illustrate the potential of elastic domains for hosting exceptional points with enhanced sensing capabilities. However, a treatment from a fundamental structures perspective is still missing, along with potential implementations related to sensing and detection. Towards bridging this gap, we investigate 1D and 2D PT symmetric elastic domains and illustrate the formation of exceptional points arising from the introduction of balanced gain and loss elements. In particular, we first investigate 1D elastic waveguides featuring a PT symmetric pair of ground springs with complex stiffnesses, and illustrate how a large number of exceptional points naturally appear in their vibrational spectra. We investigate their sensitivity to perturbations in the form of point mass inclusions, and demonstrate both numerically and through a perturbation approach that the sensitivity has a leading term of square root order, as expected of second-order exceptional points (Chen et al., 2017; Shmuel and Moiseyev, 2020). These finding are useful when extended to 2D elastic domains, where gain and loss may be implemented through piezoelectric transducers to detect mass inclusions and surface cracks. In this context, our results open new avenues in the area of dynamic-based non-destructive testing. Changes in modal properties have long been investigated as tools to detect structural changes resulting for example from the onset of cracks. Methods based on shifts in natural frequencies provide in principle a convenient detection scheme that requires limited sensing, but they have broadly shown strong sensitivity limitations. Other techniques have explored monitoring of mode shapes and curvature shapes (Sharma et al., 2006), which while promising, suffer from high spatial measurement resolution requirements. Examples that exploit the perturbation of modal parameters, such as those caused by cracks in elastic beams and plates are illustrated in Luo and Hanagud (1997) and Sharma et al. (2006). A review of other well-establish methods for sensing and damage detection can be found in Staszewski et al. (2004) and Giurgiutiu (2007). Also, guided waves have been employed for damage detection in plates (Ruzzene, 2007) and composite materials (Kessler et al., 2002), while surface acoustic waves have been employed for sensing liquid viscosity (Jakoby and Vellekoop, 1998) and surface mass loading (Du et al., 1996). Several of these contributions exploit a linear sensitivity with respect to a perturbation parameter, which may potentially be improved in the context of exceptional points with enhanced sensitivity of square root leading order. Therefore, the findings presented in this paper may open new avenues for the general exploration of PT symmetry, exceptional points and their sensitivity in continuous elastic media, with potential applications ranging from sensors to novel structural health monitoring strategies.

This paper is organized as follows: following this introduction, Section 2 presents the analysis of PT-symmetric 1D waveguides, describing the formation of exceptional points and their sensitivity using a perturbation approach. Section 3 then presents the analysis of 2D elastic domains with PT-symmetric pairs of piezoelectric patches, where exceptional points and their sensitivity to perturbations is numerically investigated. Finally, Section 4 summarizes the main findings of the work and briefly outlines future research directions.

2. PT symmetric elastic rods

We begin our study by considering a 1D elastic waveguide equipped with a pair of ground springs (Fig. 1). We employ conceptual complex spring constants, which represent elements that introduce a gain and loss through what essentially is a feedback loop that applies restoring forces that are proportional and out-of-phase by $\pi/2$ with the displacement at their location. Their imaginary components with opposite signs induce gain and loss in equal proportions, thus making the structure PT symmetric (Domínguez-Rocha et al., 2020). We illustrate how exceptional points emerge in such a system, and investigate their sensitivity to a perturbation in the form of a point mass inclusion (M_a).

2.1. Governing equations and approximate solution approach

The equation governing the motion of the waveguide can be generally expressed as (Meirovitch, 1975):

$$\mathscr{L}[u(x,t)] - m(x)\frac{\partial^2 u(x,t)}{\partial t^2} = q(x,t), \tag{1}$$

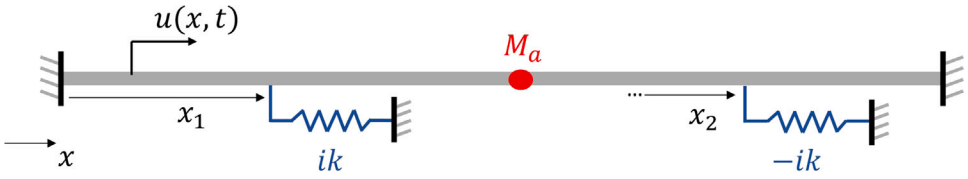

Fig. 1. Schematic of elastic rod with PT symmetric pair of ground springs and a point mass M_a attached to the center.

where $u(x,t)$ is the longitudinal displacement, $q(x,t)$ is the external loading and $m(x) = \rho A + M_a\delta(x - x_m)$ is the linear mass density. Here, ρ and A respectively denote the mass density and cross-sectional area, while M_a is the mass at location $x = x_m$ defined by the δ function. Assuming longitudinal motion, the linear differential operator $\mathscr{L}$ is given by:

$$\mathscr{L} = EA\frac{\partial^2}{\partial x^2} - \sum_{s=1}^{S} k_s\delta(x - x_s), \tag{2}$$

where E is the Young's modulus, k_s and x_s are respectively the spring constant and the location of the sth ($s = 1, \dots, S$) ground spring. While we here focus our attention to axial motion, this formulation lends itself to the analysis of other wave motion, such as flexural (transverse) vibrations for which the operator $\mathscr{L}$ includes a fourth-order derivative (Pal et al., 2019). Numerical results for flexural vibrations of elastic beams are presented at the end of this section.

We seek for approximate solutions to Eq. (1) by expressing the axial displacement through a set of N comparison functions $\phi_n(x)$

$$u(x) = \sum_{n=1}^{N} u_n\phi_n(x), \quad \phi_n(x) = \sin\left(\frac{\pi n x}{L}\right), \qquad n = 1, \dots, N, \tag{3}$$

for a rod of length L, that is fixed at bound ends, *i.e.* $u(0) = u(L) = 0$.

Assuming an external harmonic load $q(x,t) = q(x)e^{i\omega t}$, the application of Galerkin's method (Meirovitch, 1975) leads to a set of N algebraic equations, which can be expressed in the following matrix form:

$$(\mathbf{K} - \omega^2\mathbf{M})\mathbf{u} = \boldsymbol{q} \tag{4}$$

where $\mathbf{u} = [u_1, u_2, \dots, u_N]^T$, while $\mathbf{K}$ and $\mathbf{M}$ are the $N \times N$ mass and stiffness matrices, whose i,jth entries are given by:

$$\begin{aligned} k_{ij} &= \int_0^L \mathscr{L}[\phi_i(x)]\phi_j(x)dx = EA\left(\frac{i^2\pi^2}{2L}\right)\delta_{ij} + \sum_{s=1}^{S} k_s\phi_i(x_s)\phi_j(x_s) \\ m_{ij} &= \int_0^L m(x)\phi_i(x)\phi_j(x)dx = \frac{\rho AL}{2}\delta_{ij} + M_a\phi_i(x_m)\phi_j(x_m), \end{aligned} \tag{5}$$

with δ_{ij} denoting the Kronecker delta. Also in Eq. (4), $\boldsymbol{q} = [q_1, q_2, \dots, q_N]^T$ is the external load projected in the basis of the comparison functions, i.e. $q_n = \int_0^L q(x)\phi_n dx$. For the purposes of the present work, we consider a point force f applied at a location $x = x_f$, i.e. $q(x,t) = f(t)\delta(x - x_f)$, which gives $q_n(t) = f(t)\phi_n(x_f)$.

2.2. Perturbation approach

We carry out a perturbation approach to predict the frequency splitting at an exceptional point due to the perturbation associated with the point mass inclusion M_a. While we consider perturbations in the mass matrix $\mathbf{M}$ only, similar derivations can be carried out for stiffness perturbations that affect matrix $\mathbf{K}$. We consider a first order expansion of the mass matrix around $\varepsilon = 0$, where $\varepsilon = M_a/(\rho AL)$ is the non-dimensional parameter associated with the added mass. As such, the eigenvalue problem associated with the homogeneous form of Eq. (4) is rewritten as

$$\mathbf{K}\mathbf{u} = \omega^2(\mathbf{M}_0 + \varepsilon\mathbf{M}_1)\mathbf{u}, \tag{6}$$

where $\mathbf{M}_0 = \mathbf{M}|_{\varepsilon=0}$, while $\mathbf{M}_1 = \partial\mathbf{M}/\partial\varepsilon|_{\varepsilon=0}$ is the contribution due to the added mass, i.e. $m_{1_{ij}} = (\rho AL)\phi_i(x_m)\phi_j(x_m)$.

An exceptional point is a degenerate eigenvalue of algebraic multiplicity r and geometric multiplicity 1, producing a single linearly independent eigenvector. The perturbation around such type of degeneracy follows a Newton–Puiseux series of leading order $\varepsilon^{1/r}$ (Seyranian and Mailybaev, 2003), in contrast with common degeneracies producing two linearly dependent eigenvectors where the perturbation follows with leading order ε, *i.e.* $\mathcal{O}(\varepsilon)$. We here focus on second order exceptional points with $r = 2$, resulting in the following expansions of eigenvectors and eigenfrequencies

$$\mathbf{u} = \mathbf{u}_0 + \mathbf{u}_1\varepsilon^{1/2} + \mathbf{u}_2\varepsilon^1 + \mathbf{u}_3\varepsilon^{3/2} + \mathbf{u}_4\varepsilon^2 + \cdots \tag{7}$$

$$\boldsymbol{\omega} = \boldsymbol{\omega}_0 + \boldsymbol{\omega}_1\varepsilon^{1/2} + \boldsymbol{\omega}_2\varepsilon^1 + \boldsymbol{\omega}_3\varepsilon^{3/2} + \boldsymbol{\omega}_4\varepsilon^2 + \cdots \tag{8}$$

Substitution of the series expansions into Eq. (6) yields the following set of ordered equations

$$\varepsilon^0: \quad \mathbf{K}\mathbf{u}_0 = \omega_0^2\mathbf{M}_0\mathbf{u}_0 \tag{9}$$

$$\varepsilon^{1/2}: \ (\mathbf{K}-\omega_0^2\mathbf{M}_0)\mathbf{u}_1 = 2\omega_0\omega_1\mathbf{M}_0\mathbf{u}_0 \tag{10}$$

$$\varepsilon^{1}: \ (\mathbf{K}-\omega_0^2\mathbf{M}_0)\mathbf{u}_2 = \omega_0^2\mathbf{M}_1\mathbf{u}_0 + 2\omega_0\omega_1\mathbf{M}_0\mathbf{u}_1 + (\omega_1^2+2\omega_0\omega_2)\mathbf{M}_0\mathbf{u}_0 \tag{11}$$

$$\varepsilon^{3/2}: \ (\mathbf{K}-\omega_0^2\mathbf{M}_0)\mathbf{u}_3 = 2\omega_0\omega_1\mathbf{M}_0\mathbf{u}_2 + 2\omega_0\omega_1\mathbf{M}_1\mathbf{u}_0 + (\omega_1^2+2\omega_0\omega_2)\mathbf{M}_0\mathbf{u}_1 + \omega_0^2\mathbf{M}_1\mathbf{u}_1 + (2\omega_0\omega_3+2\omega_1\omega_2)\mathbf{M}_0\mathbf{u}_0 \tag{12}$$

Note that to obtain up to the second correction ω_2, equations up to $\varepsilon^{3/2}$ are needed. The ε^0 equation corresponds to the eigenvalue problem of the unperturbed system, i.e. the rod with no added mass. This eigenvalue problem is solved numerically as a function of the spring constant k to find the existence of exceptional points. A second order exceptional point produces a double eigenvalue ω_0 and a single eigenvector $\mathbf{u}_0$. The corresponding left-eigenvector $\mathbf{v}_0$ satisfying $\mathbf{v}_0^H\mathbf{K} = \omega_0^2\mathbf{v}_0^H\mathbf{M}_0$ is also obtained numerically, where $()^H$ denotes the conjugate transpose. It is useful to consider the Jordan chain of length 2 associated with the degeneracy (Seyranian and Mailybaev, 2003), i.e. $\{\mathbf{u}_0, \mathbf{w}_0\}$ and $\{\boldsymbol{\nu_0}, \mathbf{z}_0\}$, where $\mathbf{w}_0$ and $\mathbf{z}_0$ are associated (or generalized rank 2) right and left eigenvectors satisfying the equations

$$\mathbf{K}\mathbf{w}_0 = \omega_0^2\mathbf{M}_0\mathbf{w}_0 + \mathbf{M}_0\mathbf{u}_0, \qquad \mathbf{z}_0^H\mathbf{K} = \omega_0^2\mathbf{z}_0^H\mathbf{M}_0 + \mathbf{v}_0^H\mathbf{M}_0, \tag{13}$$

with the following normalization conditions

$$\mathbf{v}_0^H\mathbf{M}_0\mathbf{w}_0 = \mathbf{z}_0^H\mathbf{M}_0\mathbf{u}_0 = 1, \qquad \mathbf{v}_0^H\mathbf{M}_0\mathbf{u}_0 = \mathbf{z}_0^H\mathbf{M}_0\mathbf{w}_0 = 0. \tag{14}$$

A choice of associated eigenvectors $\{\mathbf{w}_0, \mathbf{z}_0\}$ is determined numerically by using the pseudo-inverse of the matrix $\mathbf{K}-\omega_0^2\mathbf{M}_0$. While the Jordan chain is not unique (Seyranian and Mailybaev, 2003), for a given choice of right eigenvectors $\{\mathbf{u}_0, \mathbf{w}_0\}$ the left eigenvectors $\{\mathbf{v}_0, \mathbf{z}_0\}$ are uniquely determined by the normalization conditions stated in Eq. (14). To determine the perturbed eigenvector $\mathbf{u}$ uniquely, it is convenient to consider the normalization $\mathbf{z}_0^H\mathbf{M}_0\mathbf{u} = 1$. Since $\mathbf{z}_0^H\mathbf{M}_0\mathbf{u}_0 = 1$ from Eq. (14), this gives the following conditions for the eigenvector perturbations:

$$\mathbf{z}_0^H\mathbf{M}_0\mathbf{u}_i = 0, \quad i = 1, 2, \ldots \tag{15}$$

Starting with the $\varepsilon^{1/2}$ equation, we remark that the matrix operator $\mathbf{K}-\omega_0^2\mathbf{M}_0$ is singular with rank $N-1$ due to the degeneracy at ω_0. To circumvent this issue, the normalization condition for $\mathbf{u}_1$ given by Eq. (15) is pre-multiplied by $\mathbf{v}_0$ and added to the $\varepsilon^{1/2}$ equation, yielding

$$\boldsymbol{G}\mathbf{u}_1 = 2\omega_0\omega_1\mathbf{M}_0\mathbf{u}_0, \tag{16}$$

where $\boldsymbol{G} = \mathbf{K}-\omega_0^2\mathbf{M}_0 + \mathbf{v}_0\mathbf{z}_0^H\mathbf{M}_0$ becomes a non-singular matrix due to the addition of the term $\mathbf{v}_0\mathbf{z}_0^H\mathbf{M}_0$ (Seyranian and Mailybaev, 2003). The same procedure applied to the $\mathbf{w}_0$ equation (Eq. (13)) gives $\boldsymbol{G}\mathbf{w}_0 = \mathbf{M}_0\mathbf{u}_0$, which when compared to Eq. (16) (and noting that $\boldsymbol{G}$ is non-singular) gives

$$\mathbf{u}_1 = 2\omega_0\omega_1\mathbf{w}_0. \tag{17}$$

Substitution of Eq. (17) into the ε^1 equation, left multiplication by $\mathbf{v}_0^H$ and considering the normalization conditions described previously yields the $\varepsilon^{1/2}$ frequency correction:

$$\omega_1 = \pm\frac{1}{2}\sqrt{-\mathbf{v}_0^H\mathbf{M}_1\mathbf{u}_0} \tag{18}$$

Next, we establish the ε^1 order correction ω_2. To that end, the ε^1 equation is first multiplied by $\mathbf{z}_0^H$ from the left, which upon normalization gives:

$$\mathbf{v}_0^H\mathbf{M}_0\mathbf{u}_2 = \omega_0^2\mathbf{z}_0^H\mathbf{M}_1\mathbf{u}_0 + \omega_1^2 + 2\omega_0\omega_2. \tag{19}$$

Now, multiplying the $\varepsilon^{3/2}$ equation by $\mathbf{v}_0^H$ from the left, and using Eq. (17), Eqs. (18) and (19), along with normalization conditions, gives

$$\omega_2 = -\frac{1}{8\omega_0}\mathbf{v}_0^H\mathbf{M}_1\mathbf{u}_0 - \frac{\omega_0}{4}(\mathbf{z}_0^H\mathbf{M}_1\mathbf{u}_0 + \mathbf{v}_0^H\mathbf{M}_1\mathbf{w}_0) \tag{20}$$

According to the equations above, we conclude that the degeneracy at ω_0 initially splits symmetrically with respect to ω_0 with a $\varepsilon^{1/2}$ dependence due to the ω_1 corrections, which are equal and opposite in sign (Eq. (18)). For higher ε values a linear correction ω_2 (depending on ε^1) becomes relevant, which is equal for both branches (Eq. (18)). The difference between the frequency of the two branches considering only the first two perturbation orders is therefore expressed as

$$\Delta\Omega = \varepsilon^{1/2}\sqrt{-\mathbf{v}_0^H\mathbf{M}_1\mathbf{u}_0} \quad , \tag{21}$$

since the ω_1 correction is the same for both branches. As further described in the next section, the frequency splitting $\Delta\Omega$ is a parameter commonly used for sensing, which is said to be *enhanced* due to the dependence on $\varepsilon^{1/2}$ (Hodaei et al., 2017; Chen et al., 2017; Kononchuk and Kottos, 2020; Shmuel and Moiseyev, 2020).

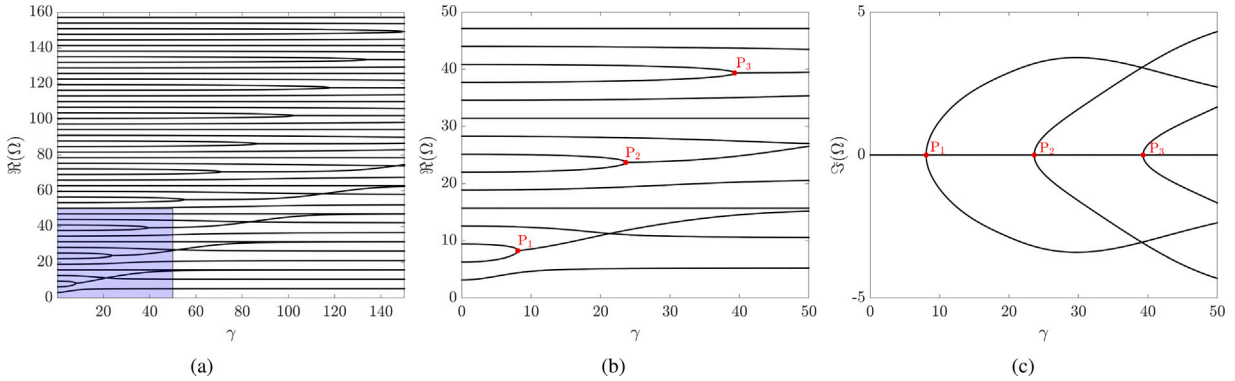

Fig. 2. Eigenfrequencies of PT-symmetric rod as a function of γ. The real components for the first 50 modes are displayed in (a) illustrating the presence of several exceptional points. In (b,c), the real and imaginary eigenfrequency components are respectively displayed zoomed in the shaded blue region of (a).

2.3. Numerical results and analysis

The elastic waveguide has two ground springs attached to locations x_1 and x_2, with spring constants $k_1 = ik$ and $k_2 = -ik$ (Fig. 1). To guarantee PT symmetry, we consider $x_2 = L - x_1$, such that the locations of the ground springs are symmetric with respect to the center, where the mass M_a is attached ($x_m = L/2$). The role of parity is to produce spatial inversions, say with respect to the center $x = L/2$, which when combined with time reversal ($i \to -i$) produces the same structure and operator, confirming the PT-symmetry. As expected (Bender and Boettcher, 1998), we find that the eigenvalues of the PT-symmetric rod are either real or come in complex conjugate pairs, and exceptional points are found defining a transition from the first case to the latter as the spring constant k is varied. In our numerical simulations, we consider $x_1 = 0.2L$ and a set of $N = 400$ basis functions in Eq. (3). Results are displayed in terms of non-dimensional frequency $\Omega = \omega/\omega_0$, with $\omega_0 = \sqrt{E/(\rho L^2)}$, and non-dimensional ground spring stiffness $\gamma = k/k_0$, where $k_0 = EA/L$ is a measure of the rod stiffness.

Fig. 2(a) displays the real part of the numerically computed eigenfrequencies for the first 50 modes of the PT symmetric rod as a function of γ. A notable feature is the presence of several exceptional points (EPs) occurring at increasing values of γ for modes of increasing order. In Figs. 2(b,c), the real and imaginary eigenfrequency components are respectively displayed zoomed in the region of the first three exceptional points (blue shaded region in Fig. 2(a)), and are labeled as P_1, P_2 and P_3. Note that these points mark the transition from the region where the two branches forming the EP are purely real, to the region where they become complex conjugate. This is usually referred to as a PT phase transition, from the unbroken (purely real) to the broken (complex conjugate) PT phases (Bender et al., 2013). For a continuous medium, the spectrum exhibits several PT phase transitions occurring for different values of γ.

In Fig. 3, we illustrate the variation of the mode shapes in the vicinity of the first two exceptional points. In particular, Figs. 3(a,c) display zoomed views of the first and second EPs, where solid black and dashed blue lines differentiate the two branches obtained from the numerical solution. Mode shapes corresponding to the points marked in Figs. 3(a,c) are displayed in Figs. 3(b,d), where each panel displays the two mode shapes for a particular γ, respectively denoted by the solid black and dashed blue lines representing the corresponding line type in (a,c). As γ increases, the modes hybridize and coalesce at the EP, where, as expected, they become identical. After the exceptional point, the two modes seem to be inverted copies of each other with respect to the center of the rod, although we dot not explore this property in further detail. We remark that the modes forming the EPs are naturally dependent on the location of the PT-symmetric inclusions. For the current example with the springs located at $x_1 = 0.2L$ and $x_2 = 0.8L$, the first EP is formed through the coalescence of the second and third vibration modes, while the second EP is formed by the 7th and 8th modes. The reader can verify in Fig. 3 that, for $\gamma = 0$, these modes have high amplitude at the locations of the springs, which facilitates their hybridization and the formation of the EP. In contrast, some modes are not modified by the presence of the springs (straight lines in Fig. 2), as they have nodes at these locations. In the Appendix section, the reader can find examples of different EPs formed with different locations of the PT-symmetric pair of ground springs.

As mentioned previously, the PT symmetric pair of springs introduce gain and loss, which in the unbroken PT phase are balanced and result in purely real eigenfrequencies. This behavior can be elucidated by analyzing the energy dissipated or provided to the system by the springs. Assuming harmonic motion, the work done by a spring in one cycle ($t = \{0, 2\pi/\omega\}$) is $W_s = \pm k\pi U^2$, where U is the amplitude of displacement at the location of the spring, and the $\pm$ signs are associated with loss and gain. For the resonances in the unbroken PT phase, the springs have the same amplitude of displacement (see modes in Fig. 3), and thus gain and loss are indeed balanced.

Next, we explore the sensitivity of the EPs to the point mass inclusion M_a. In Fig. 4(a), we repeat the eigenfrequencies of the PT rod plotted as a function of γ (black), superimposed to the frequencies for a mass inclusion $\varepsilon = M_a/(\rho AL) = 0.5\%$ (red). This very small inclusion in general introduces small changes to the resonant frequencies; however, larger changes are observed around the EPs. Figs. 4(b,c) display zoomed views of the first and second EPs. In the first case (Fig. 4(b)), the exceptional point is moved to a lower value of γ, while in the second case (Fig. 4(c)) it is moved to a higher γ. Experimentally, these changes can be

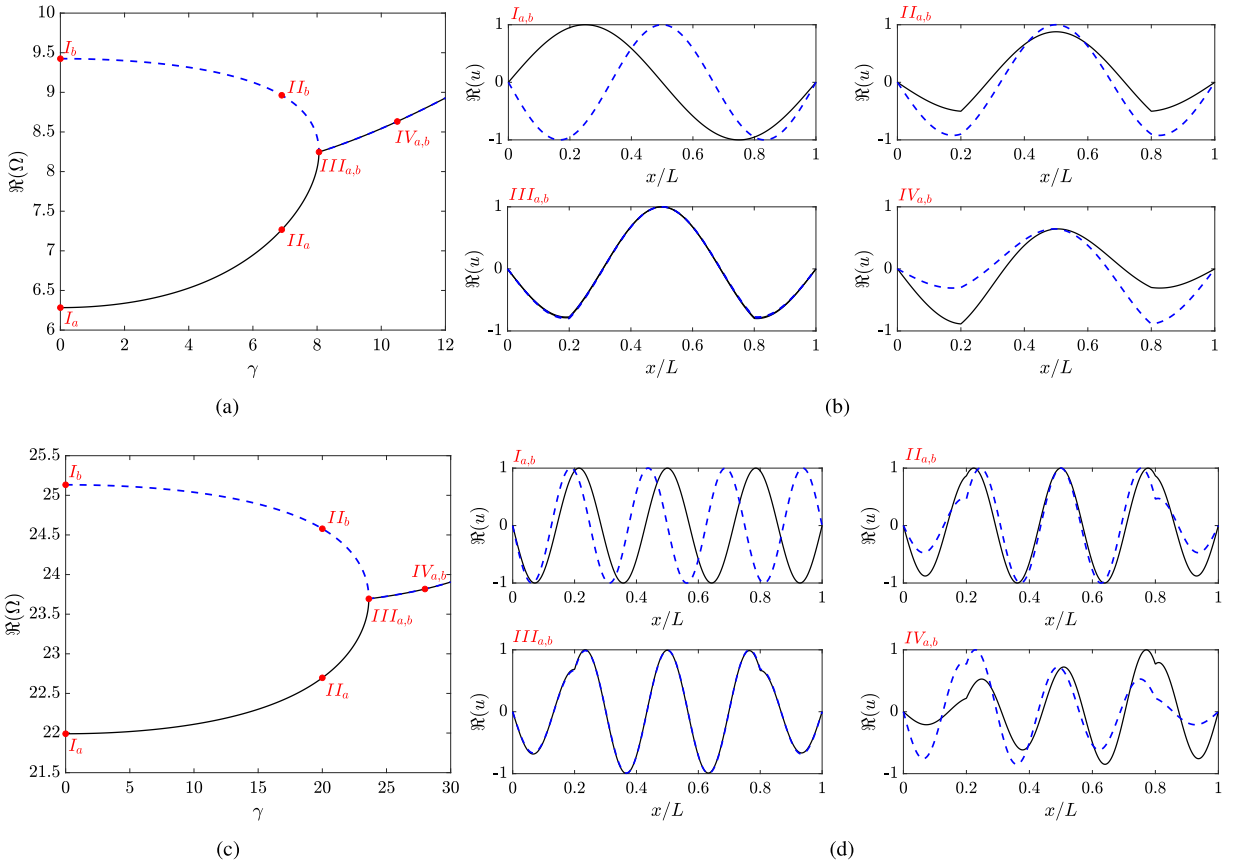

Fig. 3. Zoomed view on first (a) and second (b) exceptional points of PT symmetric rod, with variation of mode shapes for points labeled in (a,c) displayed in (b,d). Each panel in (b,d) displays two modes whose black solid or blue dashed lines represent solutions corresponding to the branches with same line type in (a,c).

detected by measuring the resonant peaks in the frequency response (Hodaei et al., 2017). This is illustrated in the right panels of Fig. 4(b,c), which display the frequency response at a point $x = 0.9L$ resulting from a point force applied at $x_f = 0.1L$, obtained from the solution of Eq. (4). Dashed blue lines are added to identify the fixed γ value used in the computation. In Fig. 4(b), this line intersects the exceptional point in the added mass case (red dot) and two distinct frequencies on the baseline case with no mass (black dots). The frequency response highlights the split of the resonant peak (red) into two distinct resonant peaks (black) matching the frequencies obtained from the eigenvalue analysis. A similar behavior is demonstrated in Fig. 4(c), except that now the dashed blue line intersects the EP for the baseline (no mass) case, and the corresponding resonant peak (black) splits into two peaks (red) upon addition of the attached mass.

The resonance split around the EPs suggest possible schemes for detection and quantification of the added mass (Hodaei et al., 2017; Chen et al., 2017; Kononchuk and Kottos, 2020; Shmuel and Moiseyev, 2020). Fig. 5(a) displays the eigenfrequencies of the PT rod as a function of γ for the second exceptional point, for $\varepsilon \in [0,\ 0.5\%]$. The shaded blue plane corresponds to $\gamma = \gamma_0$ defining the EP for $\varepsilon = 0$, and its intersection with the frequency plots highlight the frequency split as a function of ε (red dots). Indeed, the frequency difference $\Delta\Omega$ corresponding to the split can provide a way to quantify $\varepsilon = M_a/(\rho AL)$, as illustrated in Fig. 5(b), showing potentials for higher sensitivity due to the $\varepsilon^{1/2}$ dependence. For comparison, the eigenfrequencies bifurcating from the EP are repeated in the top panel of Fig. 5(c), along with the predictions given by the perturbation approach (solid curves). Specifically, the black curve corresponds to the $\varepsilon^{1/2}$ approximation, while the blue curve contains also the ε^1 dependence. While higher order terms would be required for complete agreement, the perturbation approach produces a good match considering terms up to ε^1, and confirms the expected dominant dependence upon $\varepsilon^{1/2}$ for $\varepsilon \ll 1$. The frequency splitting $\Delta\Omega$ as a function of the perturbations is often considered as the main sensing parameter (Hodaei et al., 2017), and is displayed in the bottom panel of Fig. 5(c), with the black line corresponding to the prediction given by the perturbation approach (Eq. (21)). The change in such parameter is theoretically infinite at the onset of the splitting, i.e. $\lim_{\varepsilon\to 0} \partial\Delta\omega/\partial\varepsilon = \infty$, which is of course limited by the resolution of the frequency measurements (Shmuel and Moiseyev, 2020).

The presented approach can also be applied to other 1D waveguides such as elastic beams undergoing flexural motion. This is conveniently done by employing Euler–Bernoulli beam theory, where the operator $\mathscr{L}$ defined in Eq. (2) is replaced by a fourth-order

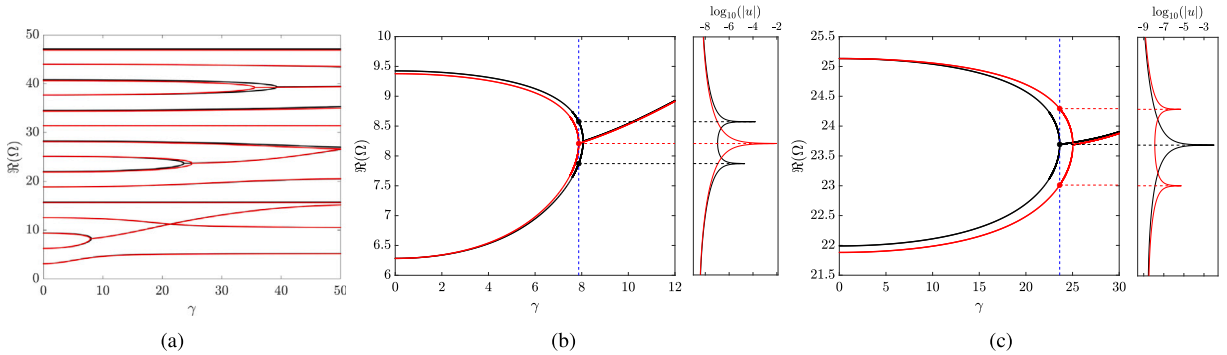

Fig. 4. Eigenfrequencies of PT symmetric rod without (black) and with (red) point mass inclusion $M_a = 0.005\rho AL$ (a), with zoomed views of the first and second exceptional points displayed in (b,c). The right panels in (b,c) display the frequency response of the rod for a fixed γ value (dashed blue lines) illustrating the splitting of the resonant peak of the EP into two separate peaks.

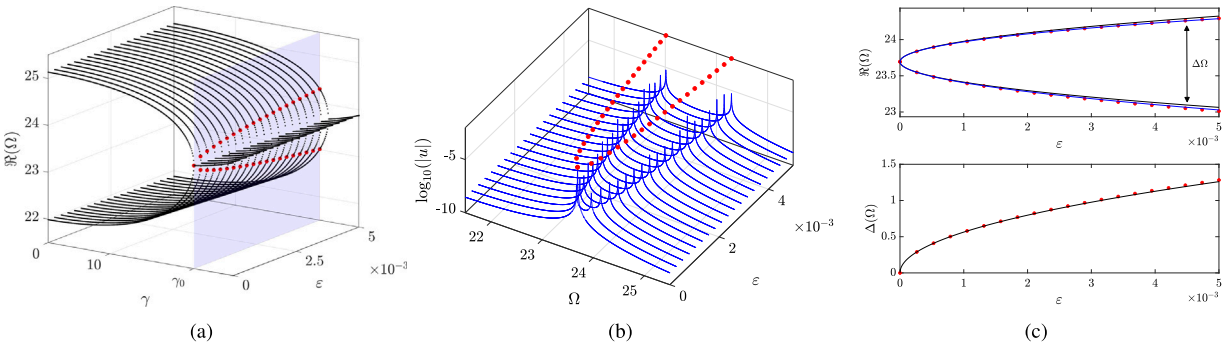

Fig. 5. Variation of EP as a function of added mass $\varepsilon = M_a/(\rho AL)$ (a). The blue plane corresponds to $\gamma = \gamma_0$ defining the EP for $\varepsilon = 0$, and intersects the frequency plots defining the frequency splitting from the EP (red dots). The frequency splitting can be measured by the variation of the resonant peaks with ε (b). The bifurcation of the EP with ε is repeated in the top panel of (c), where red dots correspond to the numerical solution, while black and blue solid curves correspond to predictions given by the perturbation approach with terms up to $\sqrt{\varepsilon}$ and ε, respectively. The frequency splitting $\Delta\Omega$ defined by the two branches is displayed in the bottom panel of (c), with the black curve corresponding to the prediction given by the perturbation approach.

operator. The described numerical procedures are then analogously applied in terms of the vertical displacement $v(x,t)$ of the beam (see Pal et al., 2019 for more details). Fig. 6 displays the results for an elastic beam equipped with the PT symmetric pair of ground springs, where non-dimensional quantities are now defined as $\Omega = \omega/\omega_0$, with $\omega_0 = \sqrt{(EI)/\rho AL^4}$, and $\gamma = k/k_0$, with $k_0 = EI/(L^3)$, while I denotes second moment of area of the beam cross section. Fig. 6(a) displays the variation of an exceptional point formed by the first two modes of the beam as a function of ε. Similarly to the case of the rods, the EP bifurcates into two branches as a function of ε (red dots), which can be detected by the splitting of resonant peaks in the forced response (Fig. 6(b)). The sensitivity of the EP is illustrated in Fig. 6(c), where both numerical results (red dots) and the perturbation analysis results (black curve) confirm the $\varepsilon^{1/2}$ dependence.

3. Guided waves in PT symmetric elastic domains

The investigations are extended to 2D elastic domains supporting guided waves. Gain and loss are now conceptually introduced through a PT symmetric pair of piezoelectric patches (Fig. 7). Piezoelectric transducers are commonly used for the generation of lamb waves (Giurgiutiu, 2007; Raghavan and Cesnik, 2005; Collet et al., 2011), for active structural control (Marconi et al., 2020; Xia et al., 2020), and, more recently, for the investigating the scattering properties of exceptional points (Wu et al., 2019; Hou and Assouar, 2018), to name a few. Therefore, they are excellent candidates for inducing gain and loss through distributions of surfaces stresses that mimic the gain and loss interactions.

3.1. Governing equations and transducer modeling

We consider a rectangular elastic domain in the x–y plane (Fig. 7) in plane strain conditions. Unit thickness along the out-of-plane direction is considered for simplicity. The top surface of the domain includes a PT symmetric pair of piezoelectric elements that induce gain and loss, in addition to two piezoelectric transducers used for actuation and sensing. The considered domain includes

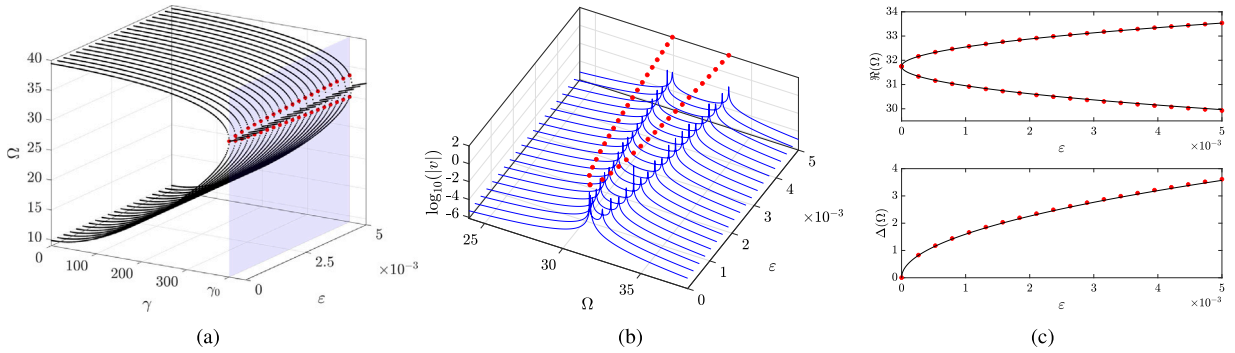

Fig. 6. Variation of EP as a function of added mass $\varepsilon = M_a/(\rho AL)$ for elastic beam (a). The blue plane corresponds to $\gamma = \gamma_0$ defining the EP for $\varepsilon = 0$, and intersects the frequency plots defining the frequency splitting from the EP (red dots). The frequency splitting can be measured by the variation of the resonant peaks with ε (b). The bifurcation of the EP with ε is repeated in the top panel of (c), where red dots correspond to the numerical solution, while the black curve corresponds to the prediction given by the perturbation approach illustrating a dependence with $\sqrt{\varepsilon}$. The frequency splitting $\Delta\Omega$ defined by the two branches is displayed in the bottom panel of (c), with the black curve also corresponding to the prediction given by the perturbation approach.

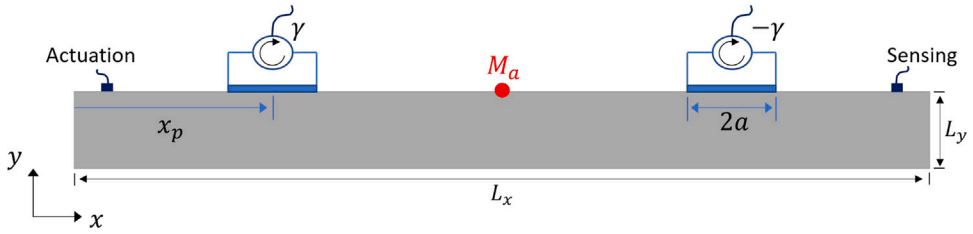

Fig. 7. Two-dimensional elastic domain (gray) with PT symmetric pair of piezoelectric patches (blue). Smaller patches (purple) are used for actuation and sensing, and point mass M_a is also attached to the top surface.

the point mass M_a also on the top surface at $x = L_x/2$. The equation of motion for the 2D domain is expressed in the frequency domain as (Graff, 2012)

$$\omega^2\rho(x,y)\mathbf{u} + (\lambda+\mu)\nabla(\nabla\cdot\mathbf{u}) + \mu\nabla^2\mathbf{u} = \boldsymbol{q}_a(x,y,t) + \boldsymbol{q}_{PT}(x,y,t) \tag{22}$$

where $\mathbf{u} = [u_x(x,y)\ u_y(x,y)]^T$ is the displacement vector field, λ and μ are lamé constants, and $\nabla = [\partial/\partial x\ \partial/\partial y]^T$. The density is expressed as $\rho(x,y) = \rho_0 + M_a\delta(x - L_x/2)\delta(y - L_y)$, where ρ_0 is the density of the domain material. Also in Eq. (22), $\boldsymbol{q}_a(x,y)$ and $\boldsymbol{q}_{PT}(x,y)$ respectively define the area forces associated with actuation and with the gain–loss transducers. The latter consist of a pair of transducers of length $2a$ deposited on the top surface of the domain, centered at locations $x_{c_1} = x_p$ and $x_{c_2} = L_x - x_p$, respectively. As previously noted, the symmetry with respect to the center is necessary to preserve PT symmetry. Their modeling follows Refs. Raghavan and Cesnik (2005) and Collet et al. (2011), which assumes their dynamics to be decoupled from that of the 2D domain, and considers their action in terms of stress components applied tangentially to the surface. Under the plane strain assumption, the $\boldsymbol{q}_{PT}(x,y,t) = [\phi(x,y,t),\ 0]^T_{y=L_y}$, where

$$\phi(x,y=L_y) = V_{0_1}(t)[\delta(x - x_{c_1} + a) - \delta(x - x_{c_1} - a) - V_{0_2}(t)(\delta(x - x_{c_2} + a) - \delta(x - x_{c_2} - a))]. \tag{23}$$

Here, the applied voltage $V_{0_i}(t)$ is defined by the difference between the $x-$component of the velocities at the edges of the piezo, i.e. $V_{0_i}(t) = \gamma(\dot{u}_x(x_{c_i}+a) - \dot{u}_x(x_{c_i}-a))$, which results from the implementation of a feedback derivative scheme with gain γ as suggested by the schematics of Fig. 7. The two additional transducers of length $2d$ and centered at locations x_a and x_s are respectively used for actuation and sensing. According to what previously described, the stress due to the piezoelectric actuation leads to the following expression for $\boldsymbol{q}_a = [q_x,\ 0^T]$, where:

$$q_x(x,y=L_y,t) = q_0(t)\delta(y - L_y)(\delta(x - x_a + d) - \delta(x - x_a - d)), \qquad q_y = 0, \tag{24}$$

with $q_0(t)$ denoting the forcing time history. For simplicity, we consider excitation of unitary amplitude $q_0 = 1$ in the frequency domain, and we measure the response at the sensing transducer as the integration of the strain ε_{xx} at the top surface over the extent of the sensor V_o (Raghavan and Cesnik, 2005), *i.e.*

$$V_o = \int_{x_s-d}^{x_s+d} \varepsilon_{xx}(x, L_y)dx. \tag{25}$$

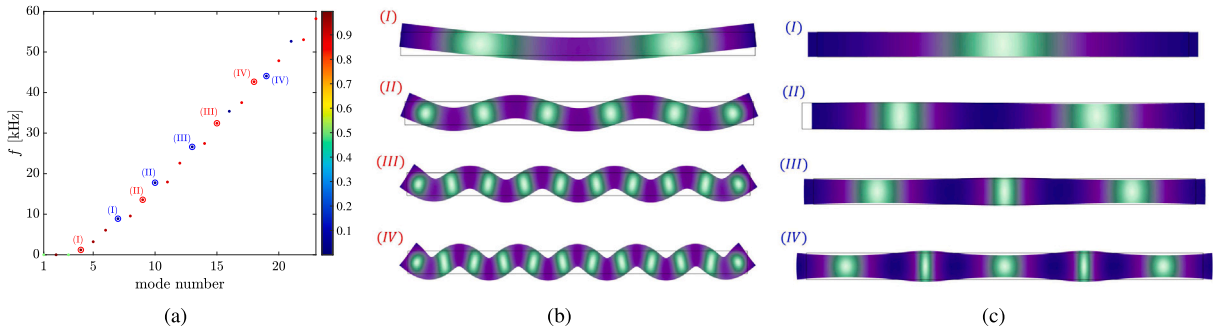

Fig. 8. Natural frequencies (a) and deformed mode shapes (b,c) for elastic domain with $\gamma = M_a = 0$. The frequencies in (a) are color-coded according to a polarization factor p that identifies modes with predominant flexural (red) or longitudinal (blue) motion.

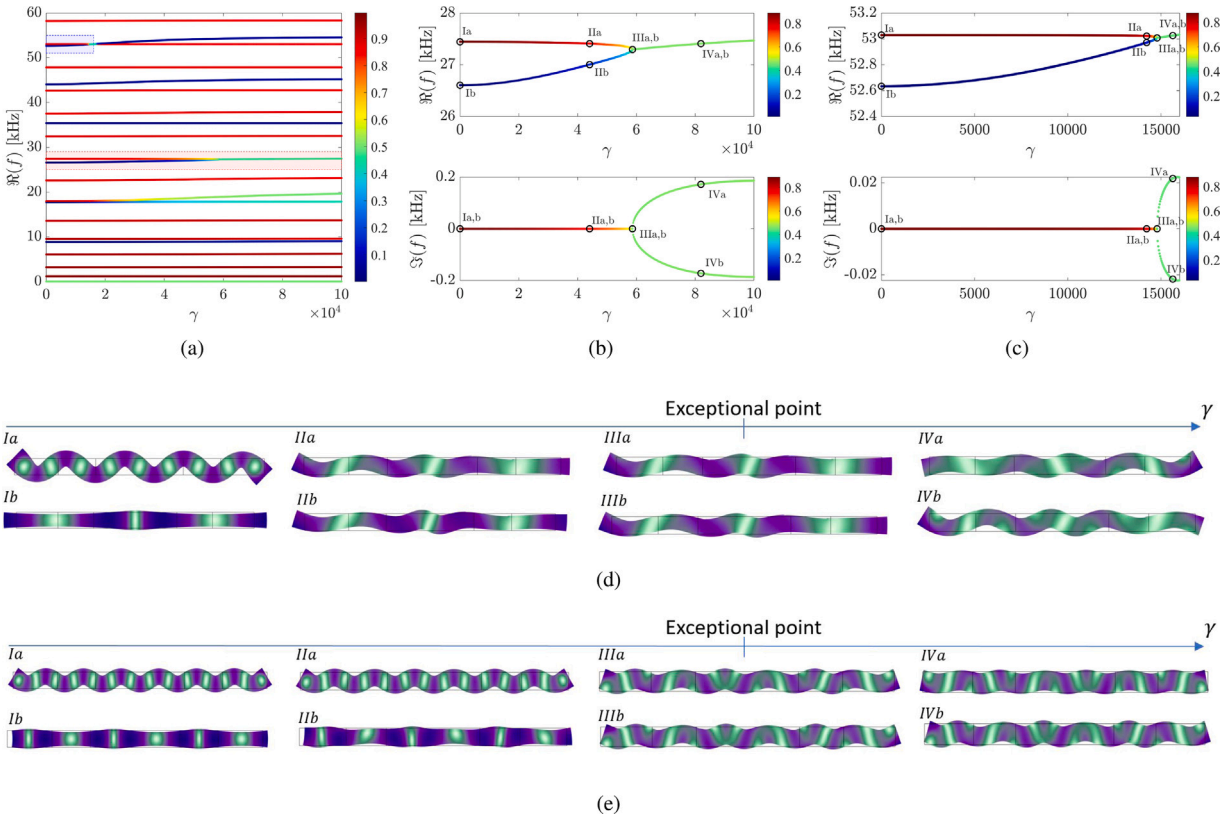

Fig. 9. Natural frequencies of 2D domain as a function of γ (a), illustrating the formation of two exceptional points. The real and imaginary frequency components of the first and second exceptional points, highlighted by the shaded red and blue areas in (a), are displayed in (b,c). The color change as the two branches in (b,c) merge indicates the hybridization between the longitudinal and flexural modes forming the EP, measured by the polarization factor p. The hybridization is further illustrated in (d,e), where deformed shapes for modes marked in (b,c) are displayed.

The resulting equation, expressed in Eq. (22), is conveniently solved using a finite element discretization of the 2D domain within the COMSOL Multiphysics environment. Specifically, under the assumption of zero external loading ($\boldsymbol{q}_a = 0$), the discretization leads to a polynomial eigenvalue problem that can be solved for eigenfrequencies and mode shapes. Consideration of the external load leads to a system that is solved in the frequency domain assuming harmoning forcing $q_{x_a}(\omega)$ at specified frequencies.

3.2. Exceptional points through hybridized Lamb modes

The 2D elastic domain (Fig. 7) is made of aluminum, with material coefficients $\lambda = 40.38$ Gpa, $\mu = 26.92$ Gpa and $\rho = 2700$ kg/m^2. The dimensions are set to $L_x = 30$ cm and $L_y = 2$ cm, with the transducers of length $2a = 4.5$ cm placed at positions $x_{c1} = 7.5$ cm

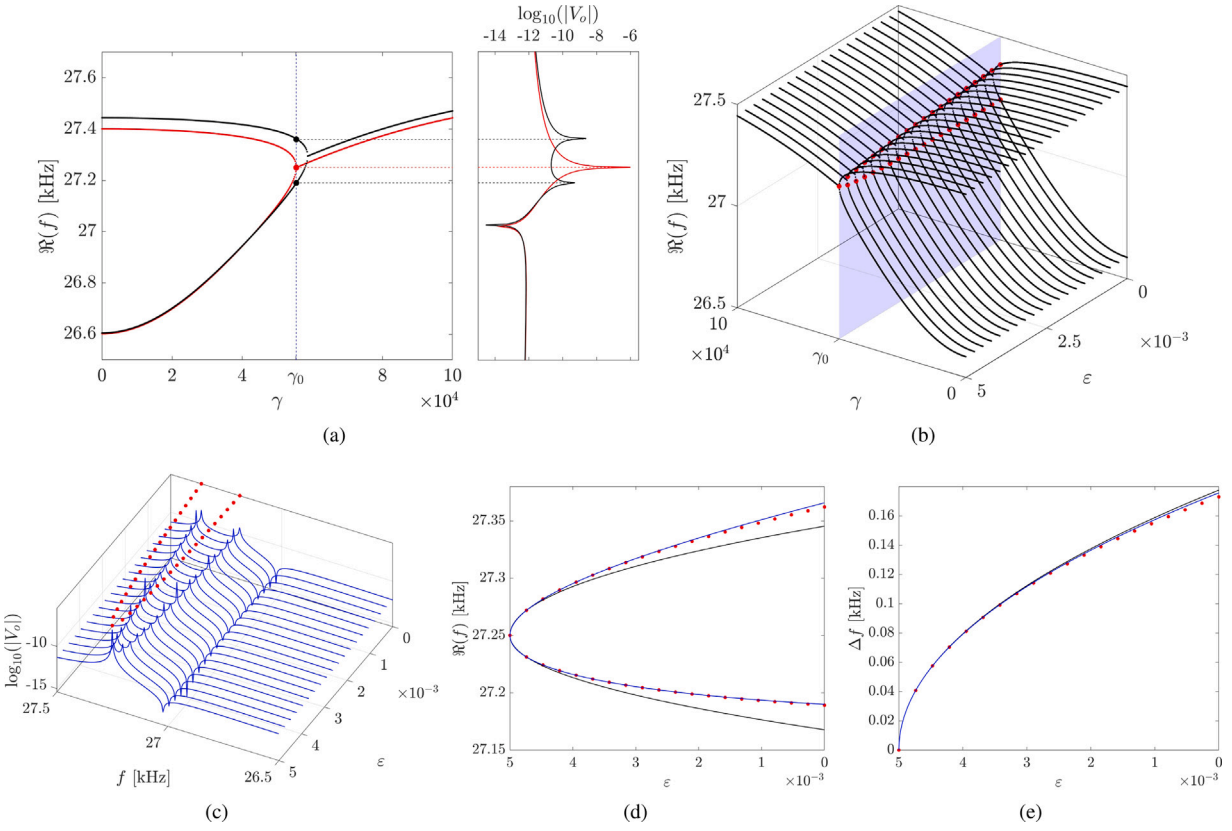

Fig. 10. Eigenfrequencies of 2D domain as a function of γ with (red) and without (black) added mass $M_a = 0.005\rho L_x L_y$ (a). The right panel displays the frequency response measured by the sensor for $\gamma = \gamma_0$, illustrating the splitting of the single (red) into two (black) resonant peaks. The variation of the EP with $\epsilon = M_a/(\rho L_x L_y)$ is displayed in (b), where the blue plane defined for γ_0 highlights the bifurcation of the EP (red dots). The splitting of the eigenfrequencies with ϵ is repeated in (c) showing good agreement with the splitting of the resonant peaks measured by the sensor. The frequency splitting is compared to polynomial fits in (d) illustrating the dependence on $\sqrt{\epsilon}$ (black), with better agreement for higher ϵ values when the linear coefficient is also included (blue). The frequency splitting Δf defined by the two branches is displayed in (e), along with polynomial fittings (solid curves) illustrating dominant dependence with $\sqrt{\epsilon}$.

and $x_{c2} = 22.5$ cm. Also, the actuation and sensing piezoelectric elements have length $2d = 0.3$ cm, and are respectively placed at positions $x_a = 1.5$ cm and $x_s = 28.5$ cm.

A 2D elastic domain of the dimensions considered supports a family of guided waves (or Lamb waves) (Graff, 2012), that propagate along the x direction in the form of symmetric (S) or anti-symmetric (A) modes. We consider traction-free boundary conditions in both x and y directions, resulting in a set of vibrating modes that are formed from standing guided waves, as illustrated in Fig. 8. In particular, Fig. 8(a) displays the first natural frequencies of the domain without any influence from the piezoelectric elements or added mass ($\gamma = M_a = 0$). Selected modes from the S0 and A0 groups are displayed in Fig. 8(b,c). These modes are tracked by considering a polarization factor p, defined as

$$p = \frac{\iint u_y^2 dA}{\iint (u_x^2 + u_y^2) dA}. \tag{26}$$

The polarization factor p is employed to color code the scatter plot in Fig. 8(a), where blue dots for $p \to 0$ correspond to predominantly longitudinal modes ($u_x \gg u_y$), while red dots for $p \to 1$ identify predominantly transverse modes ($u_y \gg u_x$). This is illustrated in the deformed shapes for selected flexural and longitudinal modes displayed in Fig. 8(b) and (c), respectively.

The variation of the corresponding frequencies with γ is displayed in Fig. 9(a). The introduction of the PT symmetric pair of piezoelectric transducers leads to the formation of two EPs in the considered frequency range, which are highlighted by the shaded red and blue areas in Fig. 9(a), while Fig. 9(b,c) display zoomed views of their real and imaginary frequency components. As expected, the EPs define a transition from a region with purely real frequencies, to a region with complex conjugate frequencies. Interestingly, both EPs are formed by the hybridization of a longitudinal (S0) and a flexural (A0) mode, as indicated by the color changes as the branches merge. This color change tracks their change in polarization as quantified by p. The deformed mode shapes for selected points marked in Fig. 9(b,c) are displayed in Fig. 9(d,e), illustrating the formation of the EP through the hybridization of the modes, with identical mode shapes occurring for the γ value corresponding to the EP.

Next, we illustrate the sensitivity of the EP to the point mass inclusion. Fig. 10(a) displays the real frequency component of the first EP for an added mass $\epsilon = M_a/(\rho L_x L_y) = 0.5\%$ (red), which is compared to the baseline case with $\epsilon = 0$ (black). Similar to the

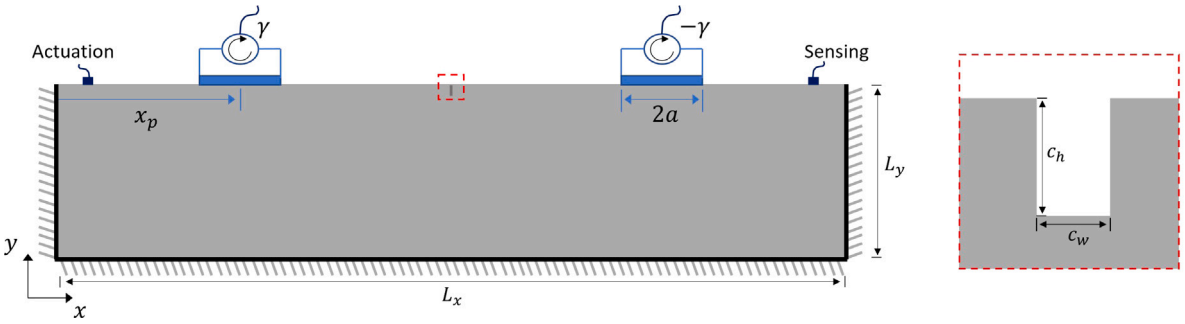

Fig. 11. Two-dimensional elastic domain with fixed boundary conditions at all edges except the top surface, where the PT symmetric pair of transducers is deposited. At the center of the top surface, a rectangular crack defect of dimensions $c_w \times c_h$ is illustrated.

first EP of the rod spectrum (Fig. 4(b)), the inclusion produces a considerable shift of the EP to a lower γ value, which we denote γ_0. Note that, in contrast to results of Fig. 5, γ_0 is chosen as the EP in the perturbed configuration instead of the unperturbed case, since the EP moves to a lower γ value with the addition of the mass. Hence, the frequency splitting will occur with the perturbed configuration as the starting point. This starting point, defined by the amount of perturbation added, is arbitrary and can be chosen based on the required ranges of specific applications. On the right panel of Fig. 10(a), the frequency response V_o measured by the sensor illustrates the splitting of the single resonant peak (red) into two separate peaks (black) occurring for $\gamma = \gamma_0$ (dashed blue line). The frequencies of the resonant peaks correspond to the eigenfrequencies for $\gamma = \gamma_0$, as illustrated by dashed red and black lines. Starting from an added mass $\epsilon = 0.5\%$, Fig. 10(b) illustrates the variation of the eigenfrequencies for decreasing ϵ values (black), highlighting the bifurcation of the EP into two branches (red dots) for $\gamma = \gamma_0$ (blue plane). The frequency splitting can be measured by the response in the sensor as illustrated in Fig. 10(c), where red dots corresponding to the numerical eigenfrequencies match the frequency of the resonant peaks as ϵ is varied. Hence, by using the frequency split of the resonant peaks measured by the sensor, one could estimate the value of an inclusion whose mass lies in the considered region. While a perturbation analysis is not conducted for this case, we illustrate in Fig. 10(d) that the splitting from the EP occurs according to the ansatz given by Eq. (7). In particular, a polynomial of the form $\omega(\epsilon) = \omega_0 + \omega_1 \epsilon^{1/2} + \omega_2 \epsilon$ can be fitted exactly to the first 3 points of each branch, resulting in the displayed solid curves. The behavior is similar to that of Fig. 5(b): the black line corresponds to the solution with only the $\epsilon^{1/2}$ dependence, showing a good agreement for lower ϵ values, while the blue line considers also the linear correction and better approximates the numerical solution for increasing ϵ values. The frequency splitting Δf is displayed separately in Fig. 10(e), with solid curves corresponding to the polynomial fits. Thus, a sensor operating in such conditions would have a high sensitivity for masses around $\epsilon = 0.5\%$, since $\partial \Delta f / \partial \epsilon \to \infty$ in that region.

3.3. Exceptional points from surface waves and crack sensing

We now consider the 2D domain depicted in Fig. 11, similar to that of Fig. 7 but with a higher height $L_y = 9$ cm and fixed boundary conditions on all edges except the top surface. This modification facilitates the formation of vibration modes concentrated at the top surface, where in addition to point mass inclusions we also consider a defect in the form of a rectangular crack of dimensions $c_w \times c_h$. The domain also includes the PT symmetric pair of transducers located at $x_{c1} = 7.5$ cm and $x_{c2} = 22.5$ cm, with length $2a = 3$ cm, and the two smaller elements for actuating and sensing as previously defined. The free surface of the 2D domain supports surface (or Rayleigh) waves (Graff, 2012), whose wave speed can be approximated as $c_r = c_s(0.87 + 1.12\nu)/(1 + \nu)$, where $c_s = \sqrt{\mu/\rho}$ is the shear wave speed, and $\nu = 0.3$ is the Poisson's ratio. This approximation gives $c_r = 2929.27$ m/s for the case at hand. We illustrate the formation of exceptional points from such surface wave modes, and their sensitivity to point mass inclusions and to the crack defect.

Fig. 12(a) displays the real and imaginary eigenfrequency components as a function of γ in the frequency range of one EP, formed by a surface wave mode and a bulk mode. The modes are differentiated by a polarization factor p_s defined as

$$p_s = \frac{\int_0^{L_x} \int_{0.75L_y}^{L_y} (u_x^2 + u_y^2) dA}{\int_0^{L_x} \int_0^{L_y} (u_x^2 + u_y^2) dA}. \tag{27}$$

Such polarization factor averages the total displacement at a region near the top surface ($y \in [0.75L_y, L_y]$), which is then divided by the total displacement integrated in the entire domain, and is employed as the color of the dots representing the eigenfrequencies in Fig. 12(a). Hence, higher values of p_s (red) signal modes with energy concentrated at the surface, while lower values of p_s (blue) indicate globally spanning modes, as verified in the mode shapes of Fig. 12(b). The modes concentrated at the surface are formed by a standing Rayleigh wave, with a small contribution from other bulk modes. For example, mode Ib in Fig. 12(b) corresponds to an eigenfrequency of $f = 141.784$ kHz. At this frequency, the non-dispersive Rayleigh waves are characterized by a

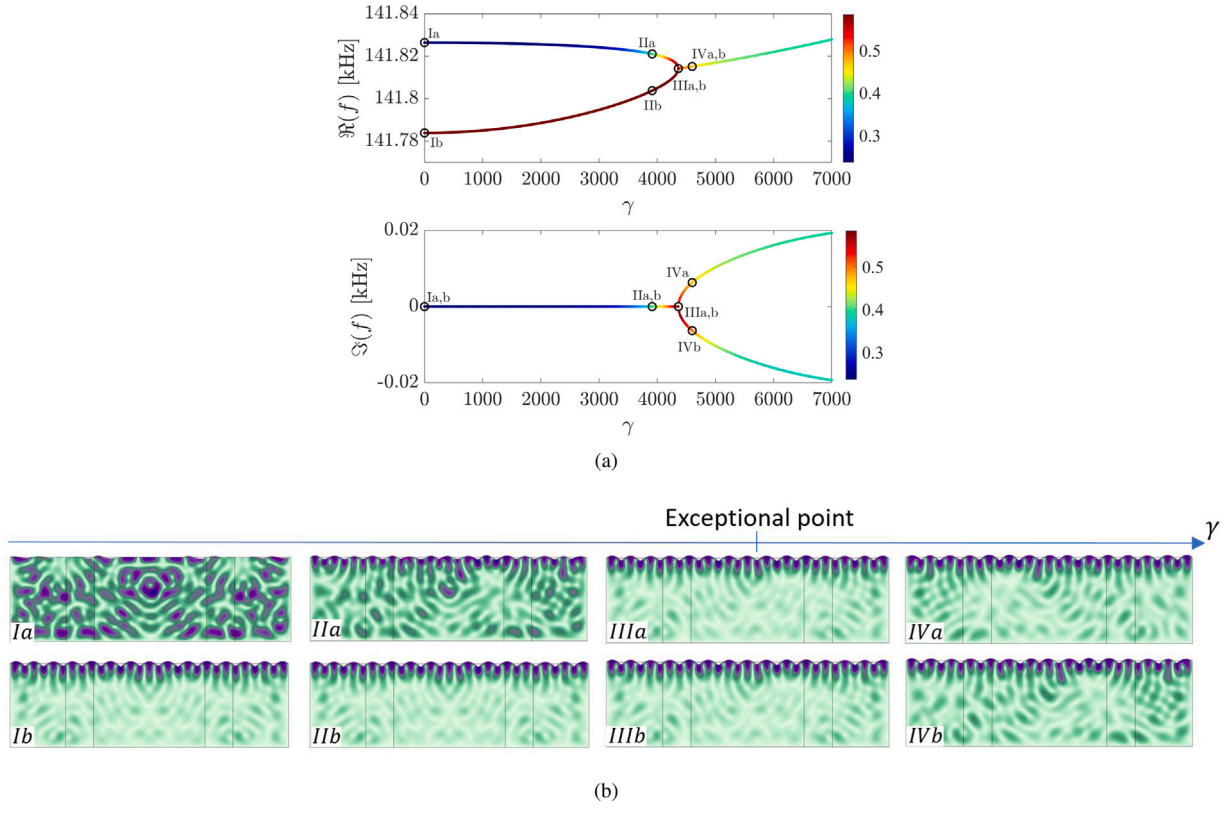

Fig. 12. Real and imaginary frequency components as a function of γ illustrating formation of the EP (a). The frequencies are color-coded according to the polarization p_s, indicating the hybridization of the surface mode (red) and the bulk mode (blue) as the EP is formed, also illustrated by the deformed mode shapes in (c).

wavelength $\lambda = c_r/f = 2.07$ cm approximately. In the domain with $L_x = 30$ cm, this mode should contain $Lx/\lambda = 14.5$ wavelengths approximately, which can be verified in its deformed shape displayed in Fig. 12(b). As γ increases, the surface mode hybridizes with the bulk mode to form the EP, as indicated by the color changes associated with p_s, and also visualized in the deformed mode shapes displayed in Fig. 12(b). At the exceptional point, both eigenfrequencies produce a single linearly independent eigenvector, constituted primarily of a surface wave mode.

Finally, we investigate the sensitivity of the EP to a point mass inclusion and to a small crack defect. Fig. 13(a) displays the variation of the EP with the added mass $\varepsilon = M_a/(\rho L_x L_y)$, while Fig. 13(d) displays the variation with the crack height $\varepsilon = c_h/L_y$, for a fixed crack width of $c_w = 32.43$ μm. The blue planes for $\gamma = \gamma_0$ highlights the bifurcation of the EP as a function of the perturbation ε (red dots). Similar to previous results, this eigenfrequency splitting may be detected by monitoring the resonant peaks split (Figs. 13(b,d)). The corresponding frequency splits Δf for the added mass and the crack are displayed in the top and bottom panels of Fig. 13(c,f), along with solid curves representing the polynomial fits previously described. Compared with previous results in this paper, we note that considerable Δf shows a larger linear dependence on the perturbation, and a smaller square root dependence, especially for the case of the surface crack. In fact, the very small crack whose width c_w approximately corresponds to 0.16% of the wavelength is sufficient to produce significant frequency splittings. This suggests that EP sensing may provide a very sensitive framework for the considered type of defect. A dominant square root dependence would be found for even smaller ε, which could generate smaller Δf values that would challenge the frequency resolution of sensing systems. These considerations will be the subject of future investigations.

4. Conclusions

In this work we have investigated elastic media such as 1D waveguides and 2D elastic domains, where PT-symmetric attachments leads to the formation of exceptional points in their vibrational spectra. We have illustrated the sensitivity of the EPs to defects such as point mass inclusions and surface cracks. In particular, the defects produce a bifurcation of the EP into two eigenfrequency branches which can be measured through the splitting of resonant peaks in the frequency response. Several opportunities are identified for future studies, such as the design of higher order EPs (Hodaei et al., 2017; Xiao et al., 2019) which provide even higher sensitivity, investigations of alternative structures and PT-symmetric gain/loss strategies, influence of noise and non-linearities and experimental demonstrations. Also, this work suggests the monitoring of resonant peaks associated with global vibration modes as

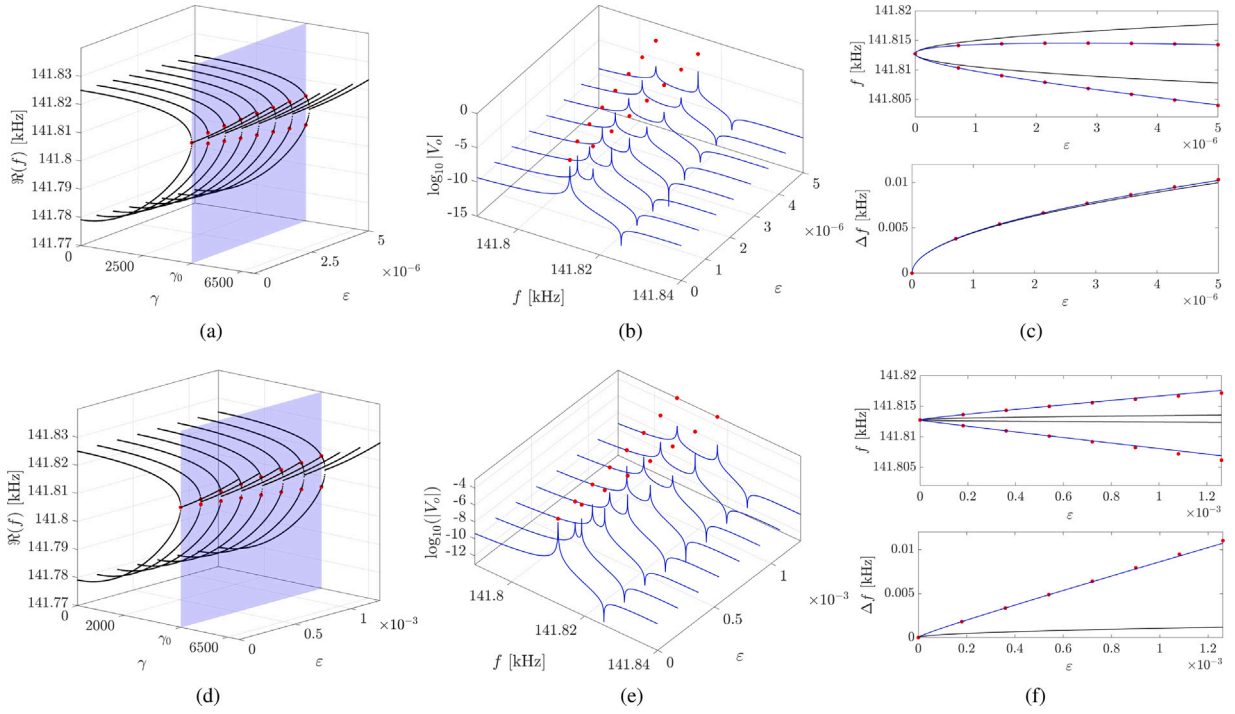

Fig. 13. Variation of eigenfrequencies forming the EP with added mass ($\varepsilon = M_a/(\rho L_x L_y)$) (a) and crack height ($\varepsilon = c_h/L_y$) (d). The blue planes defined by $\gamma = \gamma_0$ highlights the bifurcation of the EP as a function of μ_0 or c_h (red dots). The frequency response plots in (b,e) illustrate the splitting of the resonant peaks measured by the sensor, which match the splitting of the resonance frequencies. The variation of the frequencies and frequency splitting Δf with ε are displayed in the top and bottom panels of (c,f), compared with polynomial fits (solid curves).

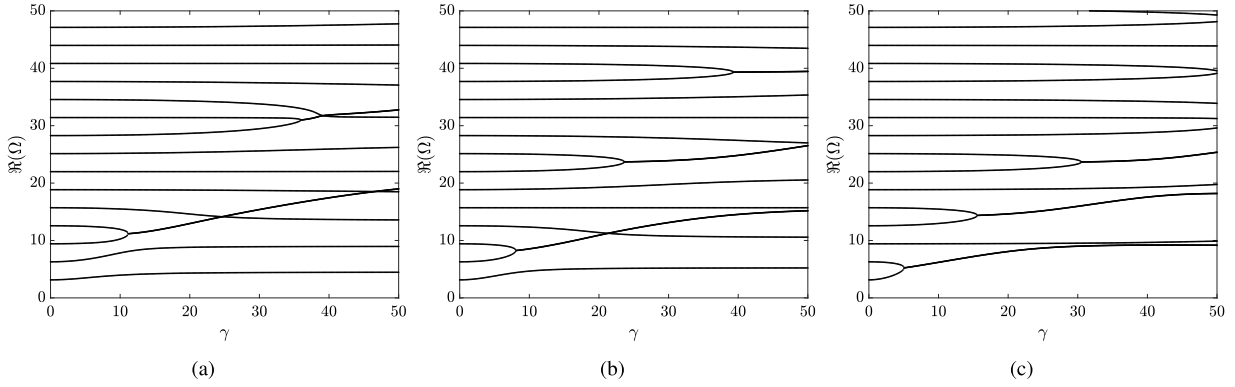

Fig. 14. Real part of eigenfrequencies as a function of γ for PT elastic rods with springs located at $x_1 = 0.15L$ (a), $x_1 = 0.2L$ (b), and $x_1 = 0.35L$ (c), illustrating the formation of EPs by the coalescence of different modes depending on the springs locations.

a detection strategy, but other methods based on wave scattering (Xiao et al., 2019) might be of significance for future work on surface waves.

Acknowledgments

The authors gratefully acknowledge the support from the National Science Foundation (NSF), USA through the EFRI 1741685 grant and from the Army Research Office, USA through grant W911NF-18-1-0036.

Appendix. Additional examples of EPs in elastic rods with different PT-symmetric springs locations

Additional examples of EPs formed in the elastic rods are reported here for different locations of the PT-symmetric pair of ground springs. The results displayed in Fig. 14 correspond to the variation of the real part of the eigenfrequencies of the rod as a function

of γ for $x_1 = 0.15L$ (a), $x_1 = 0.2L$ (b) and $x_1 = 0.35L$ (c). As noted in the main text, the location of the springs influence which modes form the EPs. For example, the first EP is formed by the 3rd and 4th modes for $x_1 = 0.15L$ (a), by the 2nd and 3rd modes for $x_1 = 0.2L$ (b), and by the 1st and 2nd mode for $x_1 = 0.35L$ (c). In general, we note that a higher number of EPs is formed at lower frequencies when the springs are closer. Although we present a few numerical results, a general rule for estimating and predicting the formation of the EPs based solely on the locations of the inclusions is still missing, and can be the subject of future investigations.

References

Ashida, Y., Gong, Z., Ueda, M., 2020. Non-Hermitian physics. arXiv preprint arXiv:2006.01837.

Bender, C.M., Berntson, B.K., Parker, D., Samuel, E., 2013. Observation of pt phase transition in a simple mechanical system. Amer. J. Phys. 81 (3), 173–179.

Bender, C.M., Boettcher, S., 1998. Real spectra in non-Hermitian Hamiltonians having P T symmetry. Phys. Rev. Lett. 80 (24), 5243.

Brandenbourger, M., Locsin, X., Lerner, E., Coulais, C., 2019. Non-reciprocal robotic metamaterials. arXiv preprint arXiv:1903.03807.

Chen, W., Özdemir, Ş.K., Zhao, G., Wiersig, J., Yang, L., 2017. Exceptional points enhance sensing in an optical microcavity. Nature 548 (7666), 192.

Christensen, J., Willatzen, M., Velasco, V., Lu, M.-H., 2016. Parity-time synthetic phononic media. Phys. Rev. Lett. 116 (20), 207601.

Collet, M., Ruzzene, M., Cunefare, K., 2011. Generation of Lamb waves through surface mounted macro-fiber composite transducers. Smart Mater. Struct. 20 (2), 025020.

Domínguez-Rocha, V., Thevamaran, R., Ellis, F., Kottos, T., 2020. Environmentally induced exceptional points in elastodynamics. Phys. Rev. A 13 (1), 014060.

Du, J., Harding, G., Ogilvy, J.A., Dencher, P., Lake, M., 1996. A study of love-wave acoustic sensors. Sensors Actuators A 56 (3), 211–219.

El-Ganainy, R., Makris, K.G., Khajavikhan, M., Musslimani, Z.H., Rotter, S., Christodoulides, D.N., 2018. Non-Hermitian physics and PT symmetry. Nat. Phys. 14 (1), 11–19.

Feng, L., Wong, Z.J., Ma, R.-M., Wang, Y., Zhang, X., 2014. Single-mode laser by parity-time symmetry breaking. Science 346 (6212), 972–975.

Fleury, R., Sounas, D., Alu, A., 2015. An invisible acoustic sensor based on parity-time symmetry. Nat. Commun. 6, 5905.

Ghatak, A., Brandenbourger, M., van Wezel, J., Coulais, C., 2019. Observation of non-Hermitian topology and its bulk-edge correspondence. arXiv preprint arXiv:1907.11619.

Giurgiutiu, V., 2007. Structural Health Monitoring: with Piezoelectric Wafer Active Sensors. Elsevier.

Gong, Z., Ashida, Y., Kawabata, K., Takasan, K., Higashikawa, S., Ueda, M., 2018. Topological phases of non-Hermitian systems. Phys. Rev. X 8 (3), 031079.

Graff, K.F., 2012. Wave Motion in Elastic Solids. Courier Corporation.

Hodaei, H., Hassan, A.U., Wittek, S., Garcia-Gracia, H., El-Ganainy, R., Christodoulides, D.N., Khajavikhan, M., 2017. Enhanced sensitivity at higher-order exceptional points. Nature 548 (7666), 187.

Hou, Z., Assouar, B., 2018. Tunable elastic parity-time symmetric structure based on the shunted piezoelectric materials. J. Appl. Phys. 123 (8), 085101.

Jakoby, B., Vellekoop, M.J., 1998. Viscosity sensing using a love-wave device. Sensors Actuators A 68 (1–3), 275–281.

Kawabata, K., Shiozaki, K., Ueda, M., Sato, M., 2019. Symmetry and topology in non-Hermitian physics. Phys. Rev. X 9 (4), 041015.

Kessler, S.S., Spearing, S.M., Soutis, C., 2002. Damage detection in composite materials using lamb wave methods. Smart Mater. Struct. 11 (2), 269.

Kononchuk, R., Kottos, T., 2020. Orientation-sensed optomechanical accelerometers based on exceptional points. Phys. Rev. Res. 2 (2), 023252.

Lee, T.E., 2016. Anomalous edge state in a non-Hermitian lattice. Phys. Rev. Lett. 116 (13), 133903.

Lin, Z., Ramezani, H., Eichelkraut, T., Kottos, T., Cao, H., Christodoulides, D.N., 2011. Unidirectional invisibility induced by p T-symmetric periodic structures. Phys. Rev. Lett. 106 (21), 213901.

Liu, T., Zhu, X., Chen, F., Liang, S., Zhu, J., 2018. Unidirectional wave vector manipulation in two-dimensional space with an all passive acoustic parity-time-symmetric metamaterials crystal. Phys. Rev. Lett. 120 (12), 124502.

Longhi, S., 2018. Parity-time symmetry meets photonics: A new twist in non-Hermitian optics. Europhys. Lett. 120 (6), 64001.

López, M.R., Zhang, Z., Torrent, D., Christensen, J., 2019. Multiple scattering theory of non-Hermitian sonic second-order topological insulators. Commun. Phys. 2 (1), 1–7.

Luo, H., Hanagud, S., 1997. An integral equation for changes in the structural dynamics characteristics of damaged structures. Int. J. Solids Struct. 34 (35–36), 4557–4579.

Marconi, J., Riva, E., Di Ronco, M., Cazzulani, G., Braghin, F., Ruzzene, M., 2020. Experimental observation of nonreciprocal band gaps in a space-time-modulated beam using a shunted piezoelectric array. Phys. Rev. A 13 (3), 031001.

Meirovitch, L., 1975. Elements of Vibration Analysis. McGraw-Hill Science, Engineering & Mathematics.

Miri, M.-A., Alù, A., 2019. Exceptional points in optics and photonics. Science 363 (6422), eaar7709.

Pal, R.K., Rosa, M.I.N., Ruzzene, M., 2019. Topological bands and localized vibration modes in quasiperiodic beams. New J. Phys. 21 (9), 093017. http://dx.doi.org/10.1088/1367-2630/ab3cd7.

Raghavan, A., Cesnik, C.E., 2005. Finite-dimensional piezoelectric transducer modeling for guided wave based structural health monitoring. Smart Mater. Struct. 14 (6), 1448.

Rosa, M.I., Ruzzene, M., 2020. Dynamics and topology of non-Hermitian elastic lattices with non-local feedback control interactions. New J. Phys. 22 (5), 053004.

Ruzzene, M., 2007. Frequency-wavenumber domain filtering for improved damage visualization. In: Ultrasonic and Advanced Methods for Nondestructive Testing and Material Characterization. World Scientific, pp. 591–611.

Seyranian, A.P., Mailybaev, A.A., 2003. Multiparameter Stability Theory with Mechanical Applications, Vol. 13. World Scientific.

Sharma, V., Ruzzene, M., Hanagud, S., 2006. Perturbation methods for the analysis of the dynamic behavior of damaged plates. Int. J. Solids Struct. 43 (16), 4648–4672.

Shen, H., Zhen, B., Fu, L., 2018. Topological band theory for non-Hermitian Hamiltonians. Phys. Rev. Lett. 120 (14), 146402.

Shmuel, G., Moiseyev, N., 2020. Linking scalar elastodynamics and non-hermitian quantum mechanics. Phys. Rev. A 13 (2), 024074.

Staszewski, W., Boller, C., Tomlinson, G.R., 2004. Health Monitoring of Aerospace Structures: Smart Sensor Technologies and Signal Processing. John Wiley & Sons.

Wu, Q., Chen, Y., Huang, G., 2019. Asymmetric scattering of flexural waves in a parity-time symmetric metamaterial beam. J. Acoust. Soc. Am. 146 (1), 850–862.

Xia, Y., Riva, E., Rosa, M.I., Cazzulani, G., Erturk, A., Braghin, F., Ruzzene, M., 2020. Experimental observation of temporal pumping in electro-mechanical waveguides. arXiv preprint arXiv:2006.07348.

Xiao, Z., Li, H., Kottos, T., Alù, A., 2019. Enhanced sensing and nondegraded thermal noise performance based on p T-symmetric electronic circuits with a sixth-order exceptional point. Phys. Rev. Lett. 123 (21), 213901.

Xiong, Y., 2018. Why does bulk boundary correspondence fail in some non-hermitian topological models. J. Phys. Commun. 2 (3), 035043.

Zhang, Z., López, M.R., Cheng, Y., Liu, X., Christensen, J., 2019. Non-Hermitian sonic second-order topological insulator. Phys. Rev. Lett. 122 (19), 195501.

Zhu, X., Ramezani, H., Shi, C., Zhu, J., Zhang, X., 2014. P t-symmetric acoustics. Phys. Rev. X 4 (3), 031042.